PUBLICATION IV

Attenuation of harmonic rotor vibration in a cage rotor induction machine by a self-bearing force actuator

In: IEEE Transactions on Magnetics 2009.
Pp. 1–12 (in press).

Attenuation of harmonic rotor vibration in a cage rotor induction machine by a self-bearing force actuator

Antti Laiho, Anssi Sinervo, Juha Orivuori, Kari Tammi, Antero Arkkio, and Kai Zenger

***Abstract*—In this paper, attenuation of flexural rotor vibration in electrical machines is considered. In order to generate force on the machine rotor, an electromagnetic actuator based on self-bearing machine working principle is examined. A control method for attenuating harmonic rotor vibration components is applied in a 30 kW two-pole cage induction machine. The machine is equipped with a four-pole supplementary winding for generation of lateral force on the rotor. Experimental results for the two-pole induction motor are presented. The main contribution of this paper is to apply a control method, specially designed for compensating harmonic excitations, by using a built-in electromagnetic actuator in an induction machine.**

***Index Terms*—induction machine, electromagnetic actuator, rotor-dynamics, self-bearing machine, bearingless drive, mechanical vibration, active control**

I. Introduction

In electrical machines, various forces of both electromagnetic and mechanical origin are acting on the rotor of the machine. Typically, these forces are harmonic with specific frequencies which depend on the design of the machine and the operation condition (number of poles, rotor bars, stator slots, rotation speed, load, saturation, possible faults etc.) [1]–[7]. Forces of the electromagnetic origin are induced by the rotating magnetic fields in the air-gap between the stator and rotor of the machine. The fields may be originated, for instance, from the stator or rotor slotting (higher harmonics), eccentric rotor motion, saturation of magnetic materials or unipolar flux (two-pole machines). On the other hand, typically, the main forces of the mechanical origin in any rotating machine are (mass) unbalance forces synchronous with the rotor rotation frequency and its multiples and sub-multiples [8].

In general, the forces acting on the rotor may result in flexural rotor vibration depending on the dynamical properties of the machine. The rotor vibration may cause additional bearing wear, increased vibration levels, fatigue, or even machine break-down. Excitation forces near resonance can be especially harmful and may disturb or even preclude the machine operation. In any case, the rotor vibration poses limitations in machine design. The critical speed, in most cases set by the first flexural rotor bending mode, is a limiting factor which reduces the operating speed range. Traditionally, electrical machines are designed to operate either below the first critical speed ('stiff-rotor') or above the first critical speed ('flexible-rotor') [9]. Optimal machine design with minimal material use may lead to a slender rotor which is problematic for vibrations. For manufacturing purposes, it would be profitable to increase the machine power by extending the rotor with a fixed machine cross-section. However, this is often not possible due to the increasing vibration responses. Hence, in order to increase the machine power above certain limit, also the cross-section has to be modified, which leads to increased manufacturing costs.

In practice, passive vibration control provides means of reducing the vibration level of the rotor, which, however, includes limitations in operation near critical speed. On the other hand, in electrical machines, a force actuator installation problem arises. In order to attenuate flexural rotor vibration at low-frequency domain, the optimal actuator position would be in the middle of the rotor, which is not possible due to the small air-gap between the stator and rotor [10].

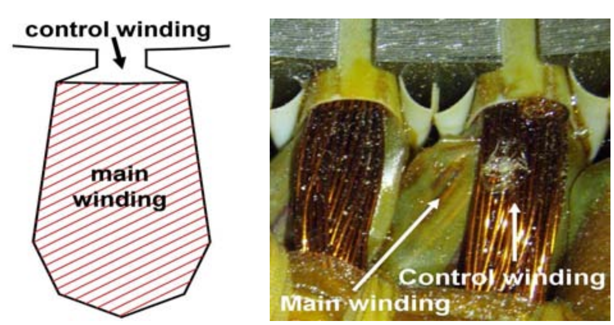

(a) (b)

Fig. 1. The control winding design in the machine stator. The control winding is distributed to the stator slots in the wedge area. In the experimental set-up of this work, the control winding occupies 10 % of the total cross-sectional area of a single slot.

During recent years, active vibration control has become an alternative for traditional passive or semi-active control methods in various industrial applications. In self-bearing (or bearingless) machine technology [11], an internal force actu-

A. Laiho is with VTT Industrial Systems, P.O. Box 1000, FIN-02044 VTT Espoo, Finland, e-mail: antti.laiho@vtt.fi

A. Sinervo is with Faculty of Electronics, Communications and Automation, Helsinki University of Technology, FIN-02015 TKK, Finland, email: anssi.sinervo@tkk.fi

J. Orivuori is with Faculty of Electronics, Communications and Automation, Helsinki University of Technology, FIN-02015 TKK, Finland, email: juha.orivuori@tkk.fi

K. Tammi is with VTT Industrial Systems, P.O. Box 1000, FIN-02044 VTT Espoo, Finland, e-mail: kari.tammi@vtt.fi

A. Arkkio is with Faculty of Electronics, Communications and Automation, Helsinki University of Technology, FIN-02015 TKK, Finland, email: antero.arkkio@tkk.fi

K. Zenger is with Faculty of Electronics, Communications and Automation, Helsinki University of Technology, FIN-02015 TKK, Finland, email: kai.zenger@tkk.fi

ation methodology was introduced [12], [13]. The principle of the actuator force production in self-bearing machines is to generate an unbalanced magnetic field distribution in the air-gap between the stator and rotor by supplying currents to a supplementary winding placed among the torque-producing stator main winding (Fig.1). A different approach by using a single winding set was proposed in [13], [14]. The bearingless machine technology provides means of producing a controlled force in the middle of the rotor which is an advantage for vibration suppression. The construction was used for vibration attenuation in a cage induction machine by using force feedback and Proportional-Integral-Derivative (PID) controller by Chiba *et al.* [15].

Typically, the main excitation forces, both of electromagnetic and mechanical origin, exerted on the rotor of an electrical machine are rotating with specific frequencies. Hence, a narrow frequency-band controller compensating discrete dominating harmonics of the disturbance force would be potential for rotor vibration suppression in electrical machines, in general. For compensating these harmonic excitation forces, the mass unbalance compensation algorithms, or Synchronous Response Control (SRC) algorithms, were developed [16]–[23]. Previously, such controllers have mainly been used for rotor-bearing systems, Active Magnetic Bearings (AMBs) and helicopter rotors, for instance. The SRC has proven to be advantageous in AMBs [24] but has not previously been demonstrated in rotor vibration attenuation by using a self-bearing force actuator in an induction machine.

In this paper, we apply a SRC algorithm referred to as 'Convergent Control' (CC) [19] in a 30 kW two-pole cage induction machine equipped with a four-pole supplementary winding for generation of lateral force on the rotor. A two-pole cage induction machine was chosen for the reason that they are generally known to have rotor vibration problems [9]. Previously, CC algorithm was systematically compared to other algorithms for flexural rotor vibration suppression [25]. Motivated by the results, CC algorithm was chosen for this work.

Furthermore, in this work, a voltage-fed actuator design is examined. Previously, a current-fed actuator was considered by Chiba *et al.* [15]. In the voltage-fed system, additional dynamics is involved due to the RL -circuit of the supplementary winding. On the other hand, the damping properties of the short-circuited supplementary winding are readily available. Identification of the system in frequency-domain is discussed. Furthermore, experimental results are presented in which CC algorithm was used for compensation of harmonic excitation forces of both electromagnetic (magnetic pull due to eccentric rotor) and mechanical (mass unbalance harmonics) origin.

II. The built-in force actuator

The working principle of the built-in force actuator is to generate an additional magnetic field component which unbalances the field distribution in the air-gap between the stator and rotor so that a net force is exerted on the rotor [11], [12]. In a machine with p pole pairs, the criteria for the force production is that an additional magnetic field with either $p-1$ or $p+1$ pole pairs is generated [26]. In this paper, we consider a two-pole induction machine equipped with a four-pole supplementary winding referred to as 'control winding'. Both windings are distributed symmetric 3-phase integral-slot series-connected (no parallel paths) windings. In Fig.2, the winding schema of the machine is depicted. In the figure, the phase zones of the two-pole and and four-pole windings are depicted on the outer and inner circle, respectively. In the experimental set-up, the four-pole control winding occupied 10 % of the slot area (Fig.1). In Fig.3, the two-pole fundamental field with the four-pole supplementary field distribution is schematically depicted. The four-pole field is induced by the combined effect of the eccentric rotor motion and the currents in the control winding.

Fig. 2. Stator winding schema for the two-pole machine with the four-pole control winding. The measurement windings for the two-pole flux are marked by '1a' and '1b'.

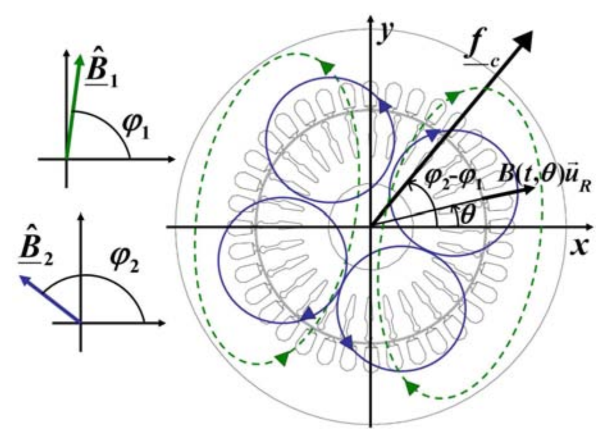

Fig. 3. Force exerted on the rotor as an effect of the two-pole (dashed line) and the four-pole (solid line) magnetic fields.

Let us denote the space-vectors of the two-pole and four-pole flux densities by $\underline{\hat{B}}_1$ and $\underline{\hat{B}}_2$, respectively [27]. Here, the sub-indices '1' and '2' refer to the two-pole (single pole-pair) and four-pole (two pole-pairs) quantities, respectively. It is assumed that the machine is under the constant-flux operating condition i.e.

$$\underline{\hat{B}}_1(t) = \hat{B}_1 e^{j\varphi_1(t)},\ \dot{\varphi}_1 = \omega_1 \quad (1)$$

where t denotes time, ω_1 the constant supply frequency (rad/s) of the two-pole winding and $\hat{B}_1$ the constant peak value of the radial two-pole flux density in the air-gap. The four-pole space-vector $\underline{\hat{B}}_2$ is a function of time and generally depends on the control winding currents and the eccentric rotor position [3], [28].

In the stator frame of reference (Fig.3), the radial magnetic flux density in the air-gap, $B(t,\theta)\vec{u}_R$, induced by the two- and four-pole fields is given by

$$B(t,\theta) = \mathrm{Re}\{\underline{\hat{B}}_1(t)e^{-j\theta} + \underline{\hat{B}}_2(t)e^{-j2\theta}\} \tag{2}$$

where θ is the angular coordinate. Typically, the tangential component of the air-gap field is considerably smaller than the radial one [29], and hence, the lateral force exerted on the rotor is obtained from the Maxwell stress tensor as

$$\begin{aligned} \underline{f}_c(t) &= \frac{d_r l_r}{2}\int_0^{2\pi}\frac{B(t,\theta)^2}{2\mu_0}e^{j\theta}\,\mathrm{d}\theta \\ &= \frac{\pi d_r l_r}{4\mu_0}\hat{B}_1 e^{-j\varphi_1(t)}\underline{\hat{B}}_2(t) \end{aligned} \tag{3}$$

in which μ_0 is the permeability of free space, d_r is the diameter of the rotor core and l_r is the length of the rotor core. Substitution of

$$\underline{\hat{B}}_2(t) = \hat{B}_2(t)e^{j\varphi_2(t)} \tag{4}$$

to Eq.(3) shows that, at time instant t, the force is directed to $\varphi_2(t) - \varphi_1(t)$ (Fig.3).

The major dynamics of the eccentric-rotor cage induction machine equipped with the built-in force actuator is governed by (i) eccentric rotor, (ii) control winding, (iii) rotor-dynamics of the flexible rotor. A Linear Time-Invariant (LTI) model of such a system with some simplifications (no saturation, no parallel stator paths etc.) was constructed in the previous paper [28]. In this model, the voltage-flux equations were formulated for the control winding and rotor cage. In addition, a model of the eccentric rotor [3] was applied. The model [28] is analogous with the actuator-rotor LTI model developed for the AMBs [30].

The controller used in this work operates in frequency domain and, in terms of system identification, requires estimates of the system Frequency-Response Functions (FRFs) at discrete frequencies. This is, a complete system model is not needed. For this reason, in this paper, the parametric model [28] is applied only for modulation of the currents and voltages in order to obtain an LTI system. Indeed, as can be seen from Eq.(3), the DC component of the control winding input voltage (generating a static four-pole field with constant $\underline{\hat{B}}_2$) induces a force revolving with angular frequency ω_1 in negative direction (clock-wise), and hence, the response (rotor displacement) is not static as it should be for an LTI system. Consequently, the actuator-rotor system is not directly LTI but, fortunately, can be transformed to an LTI system by a simple modulation of the supply voltage and the rotor cage and control winding currents [11], [28].

Let us denote the space-vector of the 3-phase control winding voltage supply by $\underline{\hat{u}}_c$. Hence, the modulated control winding supply $\underline{\hat{u}}_{c,0}$ is given by

$$\underline{\hat{u}}_{c,0}(t) = \underline{\hat{u}}_c(t)e^{-j\varphi_1(t)}. \tag{5}$$

Then, the DC component of the voltage supply $\underline{\hat{u}}_{c,0}$ results in $\underline{\hat{B}}_2$ rotating with a constant angular frequency $\dot{\varphi}_2 = \omega_1$. Consequently, the static force given by Eq.(3) is generated resulting in a static rotor displacement. The actuator-rotor model [28] can be written, in the stator coordinate system, by using real-valued LTI formalism as

$$\dot{q}(t) = Aq(t) + Bv_c(t) \tag{6}$$

$$u_{rc}(t) = Cq(t) \tag{7}$$

where $v_c = (\mathrm{Re}(\underline{\hat{u}}_{c,0}), \mathrm{Im}(\underline{\hat{u}}_{c,0}))^T$ and $u_{rc} = (x,y)^T$ in which x and y are the horizontal and vertical rotor displacements, respectively (Fig.3), and T denotes transpose. For a two-pole machine, the state-vector q consists of 8 real-valued states given by

$$q = \begin{pmatrix}\mathrm{Re}(\underline{q}) \\ \mathrm{Im}(\underline{q})\end{pmatrix} \tag{8}$$

where the complex state-vector $\underline{q}$ is given by

$$\underline{q} = \begin{pmatrix} \dot{\underline{z}}_r \\ \underline{z}_r \\ \underline{\hat{i}}_{c,0} \\ \underline{\hat{i}}_{r,2,0} \end{pmatrix}. \tag{9}$$

In Eq.(9), $\underline{z}_r = x + jy$ and the modulated control winding and rotor cage currents are given by

$$\underline{\hat{i}}_{c,0}(t) = \underline{\hat{i}}_c(t)e^{-j\varphi_1(t)} \tag{10}$$

$$\underline{\hat{i}}_{r,2,0}(t) = \underline{\hat{i}}_{r,2}(t)e^{-j\varphi_1(t)} \tag{11}$$

where $\underline{\hat{i}}_c$ and $\underline{\hat{i}}_{r,2}$ are the space-vectors of the control winding current and the rotor cage four-pole current, respectively [3], [28]. The current in the control winding is driven by the control winding voltage supply and the eccentric rotor motion. The rotor cage four-pole current is induced by the eccentric rotor motion and the mutual coupling with the control winding.

In Eqs.(6) and (7), the entries of the system matrices A, B and C consist of resistances and inductances of the rotor cage and the control winding with mechanical (modal) stiffness, damping and mass terms [28]. In addition, the eccentric rotor motion induces some additional coupling factors [3] which relate the eccentricity to the induced four-pole flux density.

In a practical application, the rotor center displacement is difficult to measure because of the small air-gap between the stator and rotor. In this work, the displacement transducers were located close to the end-shields of the machine. This set-up leads to a non-collocated system which is assumed to be a good framework at the low-frequency domain when the first rotor bending mode dominates the rotor vibration.

III. Vibration control

The control scheme used in this paper is the CC algorithm originally developed for compensating harmonic excitation forces in rotating machinery [16]–[20]. The algorithm operates in frequency-domain on harmonic multiples ($k\omega_m$, $k = 0, 1, 2, \ldots$) of the rotor rotation frequency ω_m. In the algorithm, the Fourier coefficient $\hat{v}_c^k$ of the control input v_c at the frequency $k\omega_m$ is given by the recursive law

$$\hat{v}_c^k(n) = \gamma_k \hat{v}_c^k(n-1) - \alpha_k \mathcal{A}_k \hat{u}_{rc}^k(n) \tag{12}$$

where n refers to the time instant $t_n = nT_s$ with T_s denoting the sample time, and $0 < \gamma_k \leq 1$, $\alpha_k > 0$ are parameters related to the convergence of the algorithm. Furthermore, $\hat{u}^k_{rc}$ denotes the Fourier coefficient of the rotor displacement at the frequency $k\omega_m$. In this work, the 2×2 matrix $\mathcal{A}_k$ in Eq.(12) is the inverse of the system FRF given by

$$\mathcal{A}_k = \mathcal{H}(jk\omega_m)^{-1} \tag{13}$$

where the FRF matrix $\mathcal{H}$ obtained from Eqs.(6) and (7) is given by

$$\mathcal{H}(j\omega) = C(j\omega I - A)^{-1}B. \tag{14}$$

In order to calculate the Fourier coefficients $\hat{u}^k_{rc}$, an instantaneous coefficient update [25], [31] was applied. In Fig.4, the instantaneous CC adaptation and realization is shown for compensation of a single harmonic with frequency $k\omega_m$. The rotor angular coordinate θ_m with $\dot{\theta}_m = \omega_m$ is obtained from the tachometer. Hence, the instantaneous Fourier coefficient update given by

$$\hat{u}^k_{rc}(n) = e^{-jk\theta_m(n)} u_{rc}(n) \tag{15}$$

is applied. In Fig.4, the adaptation loop given by Eq.(12) is inside the dashed box. The realization of the control signal is analogous to the inverse Fourier transformation resulting in v_c given by

$$v_c(n) = 2\mathrm{Re}\left[\sum_{k=0}^{N_f} \hat{v}^k_c(n) e^{jk\theta_m(n)}\right] \tag{16}$$

where N_f is the highest harmonic to be suppressed. The control signal given by Eq.(16) is, after 2-phase to 3-phase transformation and amplification, supplied to the control winding. A detailed analysis of CC algorithm including robustness issues was carried out by Knospe *et al.* [32].

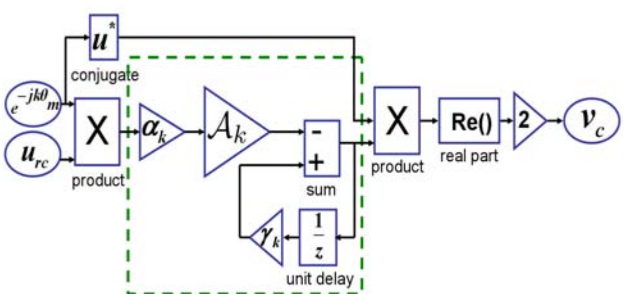

Fig. 4. The signal flow diagram of CC algorithm for a single harmonic k with an instantaneous coefficient update. In the figure, the unit delay operator is given by $z^{-1}\hat{v}^k_c(n) = \hat{v}^k_c(n-1)$.

IV. Experimental set-up

The induction motor used in the experiments is shown in Fig.5. The main parameters of the motor are listed in Table (I). The motor is a commonly-used 30 kW cage induction motor with an extended rotor shaft in order to demonstrate the low-frequency rotor vibration (Fig.6). A standard squirrel-cage rotor stack was installed on an extended rotor shaft. However, the standard squirrel-cage design induces additional dynamics to the self-bearing machine actuator. A different approach by using a pole-specific rotor construction was considered by Chiba *et al.* [33].

TABLE I
Main parameters of the induction motor used in the experiments (Fig.5). The values in parenthesis are rated values of the machine with standard rotor.

parameter	value
supply frequency [Hz]	17.0 (50)
supply voltage (rms) [V]	79.0 (400)
rotation frequency [Hz]	17.0 (49.5)
connection	delta
current [A]	15.0 (50)
rated power [kW]	30
number of phases	3
number of parallel paths	1 (2)
number of poles	2
slip [%]	0.0 (1.0)
rotor mass (rotor core and shaft) [kg]	55.80
rotor shaft length [mm]	1560
radial air-gap length [mm]	1.0
first rotor bending mode [Hz]	36.94
control winding turns per phase	240

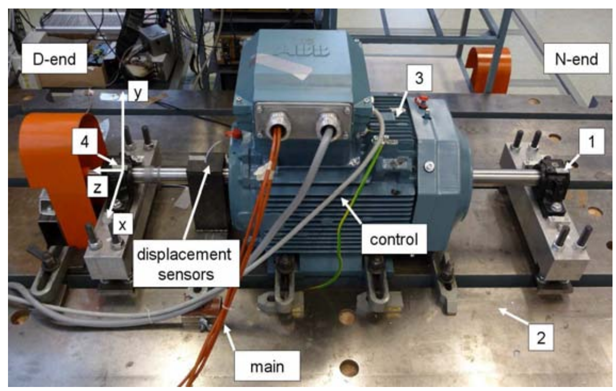

Fig. 5. The 30 kW cage induction motor used in the experiments. The numbering refers to the accelometer positions '1' (N-end bearing), '2' (foundation), '3' (stator housing) and '4' (D-end bearing) from where vibration levels were measured.

In Fig.7, a schematic picture of the experimental set-up is shown. The rotor was supported on ball element bearings at D-end (Driving end) and N-end (Non-driving end). In addition, auxiliary sliding-element bearings working as the touchdown bearings were installed with a 0.5 mm clearance inside the bearing blocks replacing the original bearings. In the experiments, the motor was supplied by a synchronous generator (17Hz and 15A supply current to the two-pole winding terminals of the motor). This gave a two-pole flux density of 0.71 T (peak value) in the air-gap (measured by two-pole flux measurement windings in the stator). The motor was run without load. In the considered operation point, the hysteresis torque of the rotor was strong enough to compensate the friction losses [34]. Consequently, the motor was running at zero slip.

The controller was operating on dSpace (DS1103 Release 4.2) real-time interface with MATLAB Real-Time Workshop. Sampling frequency of the system was set to 5 kHz. The measurement signals $\underline{e}_1$ (voltage induced in the two-pole

Fig. 6. The extended (length 1560 mm) rotor (above) used in the test machine and the standard rotor (below).

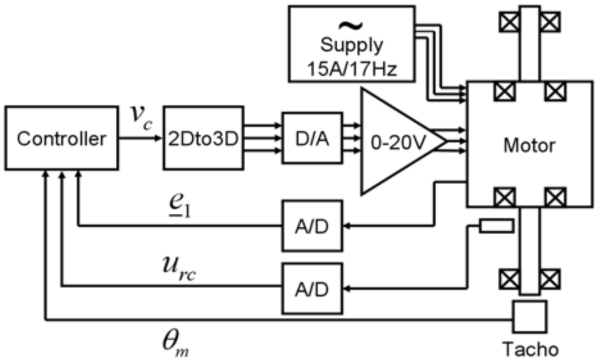

Fig. 7. Schematic view of the experimental set-up. The 2-phase to 3-phase transformation (2Dto3D) is given by Eq.(19).

flux measurement winding), u_{rc} (rotor displacement) and θ_m (rotor angular coordinate from tachometer) were transferred to dSpace. Two two-pole flux measurement windings were installed in the stator slots in order to measure

$$\underline{e}_1(t) = e_{1a}(t) + je_{1b}(t) \tag{17}$$

in which e_{1a} and e_{1b} are the voltages induced in the two-pole flux measurement windings 'a' and 'b', respectively (Fig.2). Hence, the revolving space-vector of the two-pole flux was obtained as

$$\underline{\hat{B}}_1(t) = -\frac{1}{j\omega_1 A_1 N_1}\underline{e}_1(t) \tag{18}$$

in which $A_1 = l_r d_r$ is the area and $N_1 = 2$ the number of turns of the two-pole flux measurement coil. From Eq.(18), the phase angle φ_1 of $\underline{\hat{B}}_1$ is obtained for the modulation of the input voltage in Eq.(5), which is needed for construction of the actuator-rotor LTI system given by Eqs.(6) and (7). The control signal v_c was transformed to a 3-phase voltage by the 2-phase to 3-phase transformation [27] given by

$$\begin{pmatrix} u_a \\ u_b \\ u_c \end{pmatrix} = \begin{bmatrix} 1 & 0 \\ -1/2 & \sqrt{3}/2 \\ -1/2 & -\sqrt{3}/2 \end{bmatrix} v_c. \tag{19}$$

Hence, the 3-phase voltages given by DAC outputs of the dSpace were amplified up to 20V/1.0A by amplifiers and supplied to the control winding.

A. Experimental modal analysis of the rotor

In order to obtain an insight into the mechanical characteristics of the rotor, modal testing [35] was carried out in the non-rotating case. In prior to the motor assembly, the rotor was supported by the bearings and the modal testing was performed by using an impact hammer. Total number of 8 equally distributed measurement points along the rotor shaft were used to perform the measurements. A single triaxial Endevco E65-100 accelometer fixed 15 cm from the D-end bearing was used. The hammer impacts (impact hammer Endevco E2302-5 icp) were directed in the $-y$ -direction for every measurement point. Data acquisition was performed by using Data Physics SignalCalc 240V4.7.200. Frequency resolution of the measured averaged frequency responses was 0.3125 Hz (3201 lines from 0 Hz to 1.0 kHz). The analysis was carried out in LMS Test-Lab 8A in which the PolyMAX modal parameter extraction was used. Model size was fixed to 32, and the frequency-band from 10 Hz to 900 Hz was included in the pole search. As a result, the dynamical characteristics of the rotor (natural mode shapes and frequencies) were obtained in y -direction.

The vibration modes are listed in Table (II). The first two vibration modes are shown in Fig.8. The mode 1 is the first rotor bending mode and in the mode 2 the rotor stack performs conical movement. The force actuator is capable of affecting the first mode, but, on the contrary, control of the conical mode would need a more sophisticated actuator design. The higher modes were above 480 Hz and thus beyond the scope of this work.

TABLE II
MODAL FREQUENCIES AND DAMPING RATIOS OF THE ROTOR.

mode	frequency [Hz]	damping [%]
1 (bending)	36.94	0.68
2 (conical)	203.33	0.37
3	484.95	0.87
4	518.66	1.15
5	637.39	0.58
6	668.10	0.94
7	748.38	0.89

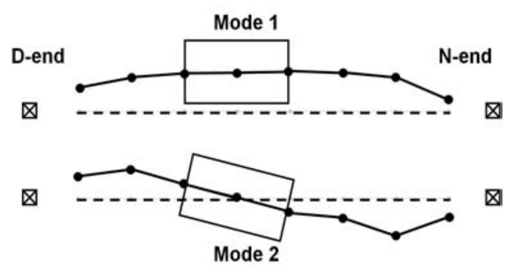

Fig. 8. Rotor shaft natural vibration modes 1 (bending) and 2 (conical). The rotor stack (box in the middle) performs rigid body movement. The undeformed rotor is marked with dashed line.

B. Modal testing by using displacement transducers

Modal testing by using an impact hammer and the displacement transducers was carried out after the motor assembly. Eddy-current displacement sensors (Bently-Nevada 3300 XL NSv Proximity Transducer System, cut-off 10 kHz) were used. The sensors measured horizontal and vertical rotor displacement close to the D-end end-shield (Fig.5). The impact point was located close to the displacement transducers. Measured FRFs are shown in Fig.9. It can be seen that, at the low-frequency range, roughly up to 70 Hz, the first bending mode

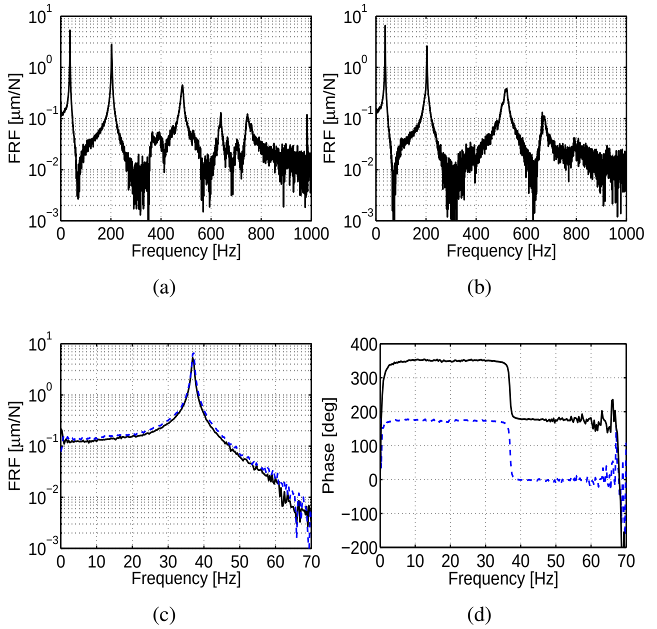

Fig. 9. Frequency responses obtained from the modal testing. (a) amplitude of FRF from f_x to x, (b) amplitude of FRF from f_y to y, (c) amplitude of FRF at low-frequency; from f_x to x (solid line) and from f_y to y (dashed line), (d) phase of FRF at low-frequency; from f_x to x (solid line), from f_y to y (dashed line). The hammer impact force f_x was in $+x$ direction and f_y in $-y$ direction (Fig.5). Hence, there is a 180 degrees phase shift in FRF from f_y to y.

dominates the dynamics of the rotor. The poles (frequencies and damping ratios), obtained from PolyMAX estimation, were at 36.94 Hz, 0.76 % (horizontal bending) and 37.12 Hz, 0.58 % (vertical bending). From the FRFs, the DC amplification gave horizontal stiffness 7.9 MN/m and vertical stiffness 7.2 MN/m. The results show that in addition to the flexible rotor, the rotor support (bearings and bearing blocks) was flexible, as well.

V. Results

A. System Identification

The aim of the system identification was to obtain valid estimates of the system transfer function $\mathcal{H}(jk\omega_m)$ in Eq.(14). The transfer function values at four harmonics ($k = 0, 1, 2, 3$) were estimated by measuring FRFs and applying black-box identification in frequency-domain by using PEM (Prediction Error Method). As a result, the method gave continuous-time system matrices A, B and C in Eqs.(6) and (7). The system order was fixed to 8 which agrees with the number of states in Eq.(8). In prior to the identification, the forced vibration peaks in the FRFs were removed by using a third order polynomial interpolation. Frequency-band included in the identification was from 1 Hz to 60 Hz.

In order to obtain FRFs for the system identification, band-limited (cut-off 500 Hz) white noise was supplied to the control winding. The first column of the frequency-response matrix $\mathcal{H}$ in Eq.(14) was obtained by supplying $\mathrm{Re}(\underline{\hat{u}}_{c,0})$ while $\mathrm{Im}(\underline{\hat{u}}_{c,0}) = 0$, and, in order to obtain the second column, $\mathrm{Im}(\underline{\hat{u}}_{c,0})$ was supplied while $\mathrm{Re}(\underline{\hat{u}}_{c,0}) = 0$. In Fig.10, the voltage input $\mathrm{Re}(\underline{\hat{u}}_{c,0})$ to the control winding is shown. The

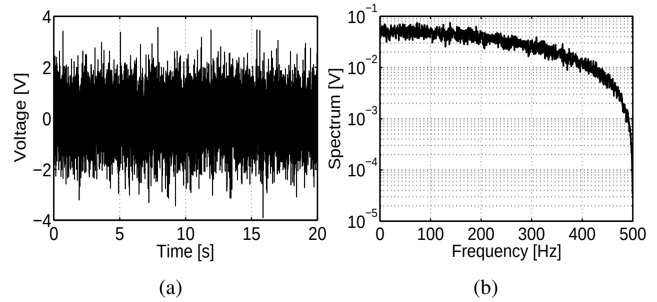

Fig. 10. Identification input voltage $\mathrm{Re}(\underline{\hat{u}}_{c,0})$. (a) Time-domain data, (b) spectrum.

TABLE III
THE POLES OF THE IDENTIFIED LTI MODEL RELATED TO THE ELECTROMECHANICAL (EM) SYSTEM AND THE RESISTOR-INDUCTOR (RL) CIRCUIT OF THE ACTUATOR.

pole	frequency f_0 [Hz]	damping ξ [%]
EM 1	32.42	41.61
EM 2	29.87	16.01
RL 1	16.74	15.28
RL 2	16.69	7.62

measured FRFs (frequency resolution 0.25 Hz) against the identified LTI model are shown in Fig.11 (magnitude) and Fig.12 (phase). The results show that the measured FRFs agree well with the FRFs obtained from the identified LTI model with 8 states. The dominating FRF peak, at 16.25 Hz, in Fig.11 is stemming from the control winding RL -resonance dynamics. Here, the 'RL resonance' refers to additional poles of the actuator-rotor system which are generated by the voltage-current relation of the voltage-fed actuator. The minor peak at 30.25 Hz is the mechanical resonance, which, compared to the modal testing results in Fig.9, is shifted in frequency and has a considerably increased damping ratio.

The poles of the identified LTI model are listed in Table (III). The poles $\underline{p}$ were obtained from the characteristic equation

$$\det(\underline{p}I - A) = 0. \tag{20}$$

The damping ratios and the frequencies were calculated from the poles by $\xi = -\mathrm{Re}(\underline{p})/|\underline{p}|$ and $f_0 = |\underline{p}|/(2\pi)$, respectively. The poles at 32.42 Hz and 29.87 Hz (FRF peak at 30.25 Hz) are related to the mechanical resonance frequencies, originally at 36.94 Hz (horizontal bending, 0.76 % damping) and 37.12 Hz (vertical bending, 0.58 % damping) in Fig.9. The reduction in frequency and increased damping can be explained by combined effect of (i) the Unbalanced Magnetic Pull (UMP) [1], [3], [36], [37] and (ii) the control winding acting as a damper winding (passive control) [15].

In a two-pole machine, the eccentric rotor motion induces a four-pole flux which crosses both the rotor cage and control winding. The four-pole flux distorts the air-gap flux distribution and induces a net force on the rotor directed approximately in the direction of the shortest air-gap (radial UMP). The radial UMP decreases the natural frequency of the rotor bending mode by the negative spring effect. In addition, the four-pole currents are induced in the rotor cage. These currents oppose the change of the four-pole flux through the

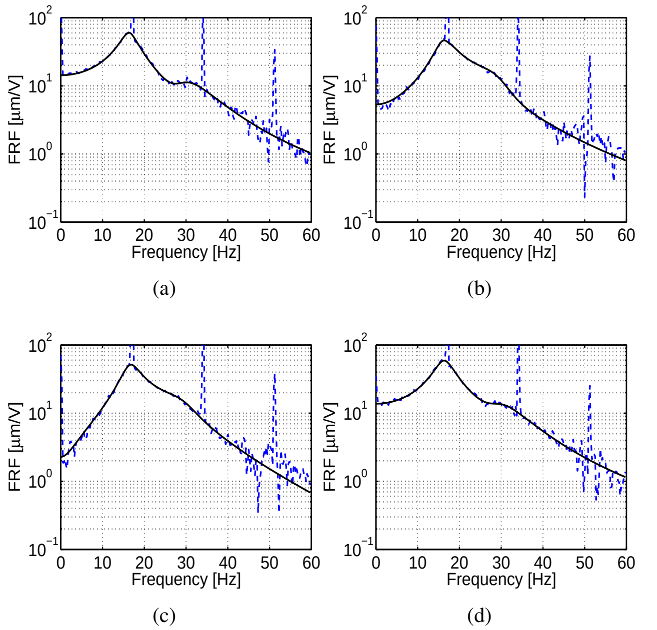

Fig. 11. Amplitudes of FRFs from measurements (dashed line) and identification (solid line); (a) from $\mathrm{Re}(\underline{\hat{u}}_{c,0})$ to x, (b) from $\mathrm{Re}(\underline{\hat{u}}_{c,0})$ to y, (c) from $\mathrm{Im}(\underline{\hat{u}}_{c,0})$ to x, (d) from $\mathrm{Im}(\underline{\hat{u}}_{c,0})$ to y.

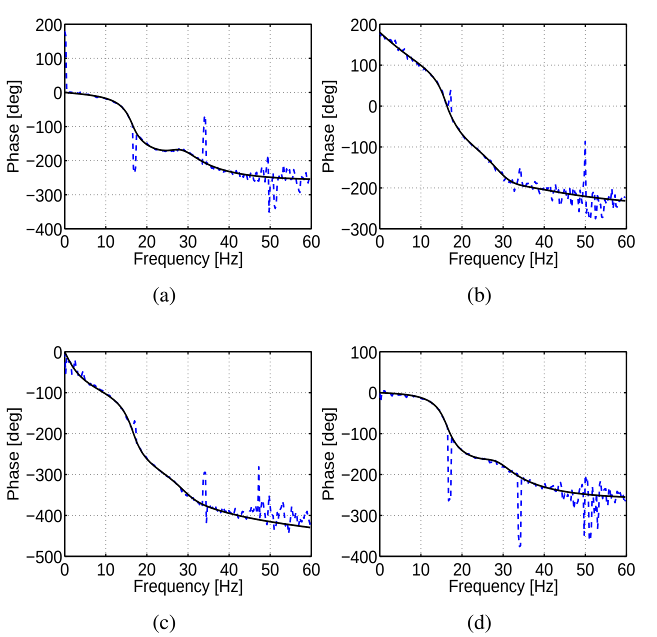

Fig. 12. Phases of FRFs from measurements (dashed line) and identification (solid line); (a) from $\mathrm{Re}(\underline{\hat{u}}_{c,0})$ to x, (b) from $\mathrm{Re}(\underline{\hat{u}}_{c,0})$ to y, (c) from $\mathrm{Im}(\underline{\hat{u}}_{c,0})$ to x, (d) from $\mathrm{Im}(\underline{\hat{u}}_{c,0})$ to y.

rotor cage and, hence, make the overall flux distribution more uniform. Consequently, the induced rotor cage currents reduce UMP and may induce a tangential UMP component [5] which has an effect on the damping of the rotor-dynamic system.

As reported previously by Chiba *et al.* [15], the short-circuited control winding acts as a passive damper for the rotor vibration. Indeed, the four-pole flux induced by the eccentric rotor motion is proportional to the product of the two-pole flux density and rotor eccentricity [3]. The four-pole flux induces a current in the control winding which opposes the change of the four-pole flux through the control winding. Consequently, the induced current is related to the rotor velocity and displacement. Hence, a net force is exerted on the rotor which affects the damping and stiffness of the rotor-dynamic system.

The poles at 16.74 Hz and 16.69 Hz (FRF peak at 16.25 Hz) in Table (III) are due to the RL -resonance of the control winding. The control winding is magnetically coupled with the rotor cage, and hence, the RL -resonance can be affected by the four-pole rotor cage currents, as well. In addition, under eccentric rotor motion, the four-pole flux (proportional to the product of the two-pole flux density and rotor eccentricity) couples with the control winding. Hence, the RL resonance peak is affected by the two-pole fundamental flux density. The damping of the poles related to the RL resonance (minimum 7.62 %) is high enough so that the phase-shift at the supply frequency (17.0 Hz) is moderate (Fig.12). This enables frequency-domain controller design without an extra compensator [28]. However, in the case of a low damping, the estimation of the system FRF would become more sensitive to changes in dynamics.

From the identified LTI model (Fig.11 and Fig.12), in the units of μm/V, the estimates for the system FRFs at $k\omega_m$, $k = 0, 1, 2, 3$ were obtained as

$$\mathcal{H}(0) = \begin{bmatrix} 14.35 & 2.36 \\ -5.38 & 13.83 \end{bmatrix} \tag{21}$$

$$\mathcal{H}(j\omega_m) = \begin{bmatrix} 57.09 \cdot e^{-j\pi \cdot 108.22/180} & 51.60 \cdot e^{j\pi \cdot 153.34/180} \\ 44.87 \cdot e^{-j\pi \cdot 16.69/180} & 56.95 \cdot e^{-j\pi \cdot 97.48/180} \end{bmatrix} \tag{22}$$

$$\mathcal{H}(2j\omega_m) = \begin{bmatrix} 9.11 \cdot e^{j\pi \cdot 153.59/180} & 8.13 \cdot e^{-j\pi \cdot 14.21/180} \\ 6.21 \cdot e^{j\pi \cdot 167.70/180} & 10.23 \cdot e^{j\pi \cdot 154.22/180} \end{bmatrix} \tag{23}$$

$$\mathcal{H}(3j\omega_m) = \begin{bmatrix} 1.78 \cdot e^{j\pi \cdot 105.63/180} & 1.52 \cdot e^{-j\pi \cdot 57.67/180} \\ 1.45 \cdot e^{j\pi \cdot 137.36/180} & 2.05 \cdot e^{j\pi \cdot 109.22/180} \end{bmatrix} \tag{24}$$

B. Passive vibration control

In Fig.13, results are shown in which a 3-phase current of 17.0 Hz, 5.2 A was supplied to the two-pole winding terminals of the motor. This generated the two-pole flux density of 0.33 T (peak value) in the air-gap. The two-pole flux density was reduced from the original 0.71 T due to the fact that the motor could not be run, without rotor touchdown with the auxiliary bearings, with control winding open and higher fundamental field. This was due to the rotor bow which emphasizes the magnetic eccentricity forces exerted on the rotor when the fundamental field is increased. In Fig.13(a), the control winding terminals were open at the beginning and abruptly, the terminals were shorted. The rotor vibration amplitudes were considerably decreased (from 203.0 μm (rms) to 61.0 μm (rms)). In Fig.13(b), under short-circuited case, the current in the control winding phase 'a' is shown. The current was dominated by 17.0 Hz (peak value 0.10 A) and 34.0 Hz (peak value 0.14 A) components which can be explained by the eccentric rotor motion (static eccentricity and rotor whirling at 17.0 Hz) with current modulation given by Eq.(10). The rms value of the current was 0.13 A.

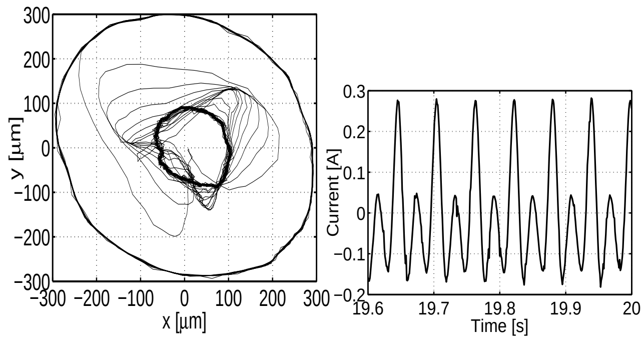

(a) (b)

Fig. 13. Control winding short circuit: (a) change of the rotor orbit when the control winding was open (outermost orbit) and then suddenly shortcut (innermost orbit), (b) current in the short-circuited control winding phase 'a' in steady-state.

C. Active vibration control

The CC algorithm given by Eq.(12) with instantaneous coefficient update (Fig.4) was employed with coefficients $\alpha_0 = 5.0 \cdot 10^{-5}$, $\alpha_1 = 20.0 \cdot 10^{-5}$ ($= T_s$, the sample time), $\alpha_2 = 10.0 \cdot 10^{-5}$, $\alpha_3 = 10.0 \cdot 10^{-5}$, $\gamma_0 = \gamma_1 = \gamma_2 = \gamma_3 = 1.0$. The FRF estimates given by Eqs.(21) - (24) were used in the adaptation given by Eq.(12). The motor was running in the operation point listed in Table (I). The two-pole flux density was 0.71 T (measured by two-pole flux measurement windings in the stator).

The rotor orbits at steady state operation with control on and control off are shown in Fig.14. The rotor orbit with control off differs from the short-circuited case in Fig.13(a) due to the higher fundamental flux. In addition, the rotor orbit at low-speed in run-down without main and control winding supply is shown. In order to obtain the slow-speed rotor orbit, the rotor was run down from a certain speed and data was collected when the rotor was rotating very slowly (0.5 Hz). Total number of 20 revolutions were averaged to obtain the rotor orbit [38].

In Fig.15, the rotor displacement is shown when the control was switched on at $t = 0.8s$. In Table (IV), the steady-state amplitudes and velocities of the rotor vibration are shown. The rotor displacement was differentiated in frequency domain up to 2 kHz from which the rms velocity values were calculated on time-domain. From the results it can be observed that the vibration of the rotor was considerably decreased.

In Fig.16, the displacement spectra of the controlled and uncontrolled systems are shown. The peak values are listed in

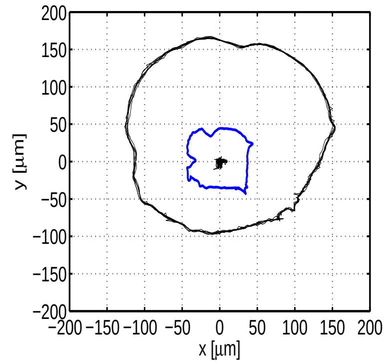

Fig. 14. The rotor orbits of the controlled system (the innermost curve), at low-speed run-down (in the middle) and the uncontrolled system (the outermost curve).

TABLE IV
VIBRATION ATTENUATION RESULTS OF CC ALGORITHM OBTAINED BY USING DISPLACEMENT TRANSDUCERS.

	control off	control on	change [%]
amplitude x (μm, rms)	98.19	2.39	-97.56
amplitude y (μm, rms)	91.33	2.35	-97.43
velocity x (mm/s, rms)	12.11	5.10	-57.92
velocity y (mm/s, rms)	11.52	4.93	-57.25

TABLE V
VIBRATION ATTENUATION RESULTS OF CC ALGORITHM OBTAINED BY USING DISPLACEMENT TRANSDUCERS: PEAK VALUES OF THE ROTOR DISPLACEMENT SPECTRA.

frequency [Hz]	0	17.0	34.0	51.0	68.0
uncontrolled x (μm)	58.3	124.1	28.7	4.4	1.1
controlled x (μm)	0.0	0.2	0.2	0.1	0.7
uncontrolled y (μm)	34.9	119.1	24.6	3.4	0.9
controlled y (μm)	0.1	0.2	0.2	0.1	0.8

Table (V). The reduction in vibration can be explained by the reduction of the DC, first, second and third component of the rotation speed. The fourth component ($4 \cdot 17.0\,\mathrm{Hz} = 68.0\,\mathrm{Hz}$) was not included into the control algorithm, and hence, the fourth harmonic peak value was not reduced. On the other hand, as can be seen from the spectrum of the uncontrolled system, the DC and the first two harmonics dominate. Hence, compensation of these low-frequency harmonics alone attenuates the rotor vibration considerably.

In Fig.17, the voltage $\underline{\hat{u}}_{c,0}$ and the voltage demand for the control winding phase 'a' is shown. The rms values for the real and imaginary parts of $\underline{\hat{u}}_{c,0}$ are 7.24 V and 6.83 V, respectively. The rms value of the voltage in phase 'a' is 3.96 V. In Fig.18, the current in the control winding phase 'a' is shown. The dominating harmonic (17.0 Hz, 34.0 Hz and 51.0 Hz) peak values for the uncontrolled system were 0.14 A, 0.34 A and 0.12 A, respectively. For the controlled system, the corresponding peak values were 0.21 A, 0.17 A and 0.05 A. The rms values of the control winding current for the uncontrolled and controlled systems were 0.31 A and 0.21 A, respectively. The higher current of the uncontrolled system can be explained by a strong influence of the eccentric rotor motion which was reduced in the controlled system.

The reaction of the control system to external excitations

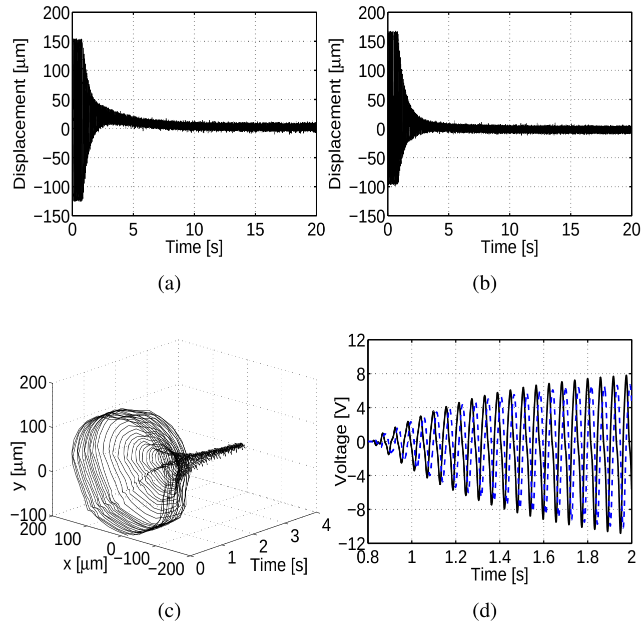

Fig. 15. The results from vibration attenuation. The control was switched on at $t = 0.8$s; (a) horizontal rotor displacement, (b) vertical rotor displacement, (c) rotor orbit, (d) control input voltage $\underline{\hat{u}}_{c,0}$: real part (solid line) and imaginary part (dashed line).

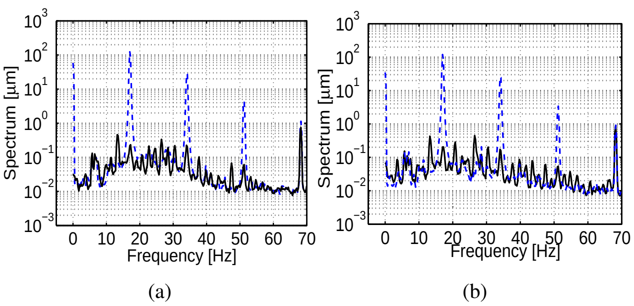

Fig. 16. Displacement spectra of controlled system (solid line) and uncontrolled system (dashed line); (a) x -direction, (b) y -direction.

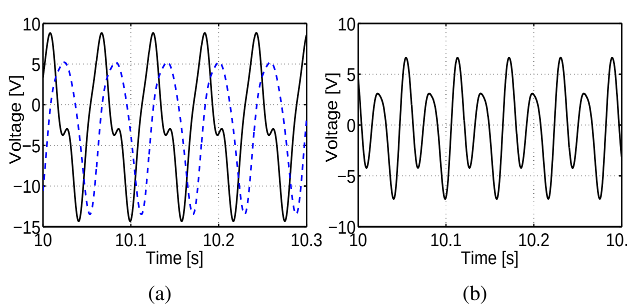

Fig. 17. Control voltage demand with control on at steady-state operating conditions. (a) The space-vector $\underline{\hat{u}}_{c,0}$; real part (solid line) and imaginary part (dashed line). (b) Phase 'a' voltage demand.

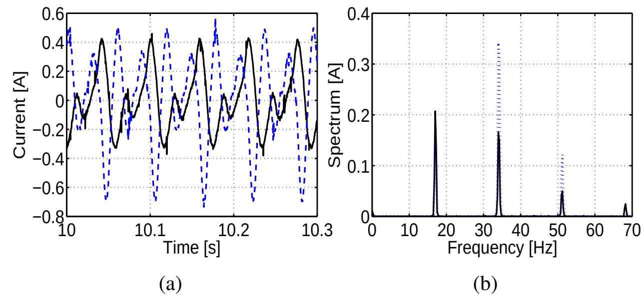

Fig. 18. Current in the control winding phase 'a'. Controlled system (solid line) and uncontrolled system (dashed line). (a) Phase 'a' current, (b) spectrum of the phase 'a' current.

was tested by hammer impacts shown in Fig.19. The results in Fig.19(a) show that the hammer impacts do not violate the controller operation. In a more detailed view, in Fig.19(b), a transient of length 0.5 s can be seen. From the spectral analysis, it can be observed that the high-frequency vibration component is at 205.5 Hz, which is, the conical rotor vibration mode has been excited (Table (II) and Fig.8).

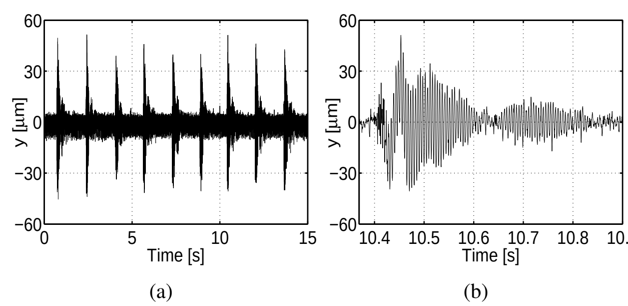

Fig. 19. Hammer impacts in $-y$ -direction on the rotor with control on; (a) multiple impacts and (b) closer look at a single impact.

TABLE VI
VIBRATION LEVELS OF THE CONTROLLED AND UNCONTROLLED SYSTEMS. THE ACCELOMETER POSITIONS '1' (N-END BEARING) , '2' (FOUNDATION), '3' (STATOR HOUSING) AND '4' (D-END BEARING) ARE SHOWN IN FIG.5.

point	direction	control off mm/s (rms)	control on mm/s (rms)	change [%]
1	x	0.76	0.41	-45.80
1	y	0.33	0.30	-10.84
1	z	1.94	1.85	-4.64
2	x	0.44	0.087	-80.10
2	y	0.31	0.074	-76.23
2	z	0.056	0.047	-16.49
3	x	0.76	0.24	-68.51
3	y	0.22	0.090	-59.00
3	z	0.078	0.068	-13.24
4	x	0.96	0.62	-35.15
4	y	0.65	0.73	+13.45
4	z	3.03	3.25	+7.26

The vibration levels of the controlled and uncontrolled system at four measurement points were measured. The measurement points '1' (N-end bearing) , '2' (foundation), '3' (stator housing) and '4' (D-end bearing) are shown in Fig.5. Triaxial Endevco E65-100 accelometers were used. Data acquisition was made in Data Physics SignalCalc 240V4.7.200

and analysis in LMS Test-Lab 8A. The velocity autopower spectra were calculated and the vibration levels (mm/s, rms) were obtained from these on the frequency band from 10 Hz to 2 kHz. The results are listed in Table (VI). In general, the vibration levels were small and they decreased when the control was switched on. However, it can be seen that, even though being of small amplitude, the vibration at point '4' (D-end bearing) in y (vertical) and z (axial) directions increased when the control was switched on. One reason for this might be the fact that the originally bowed rotor (Fig.14) was forced to the center of the displacement measurement origin. Hence, additional force may exert on the bearing.

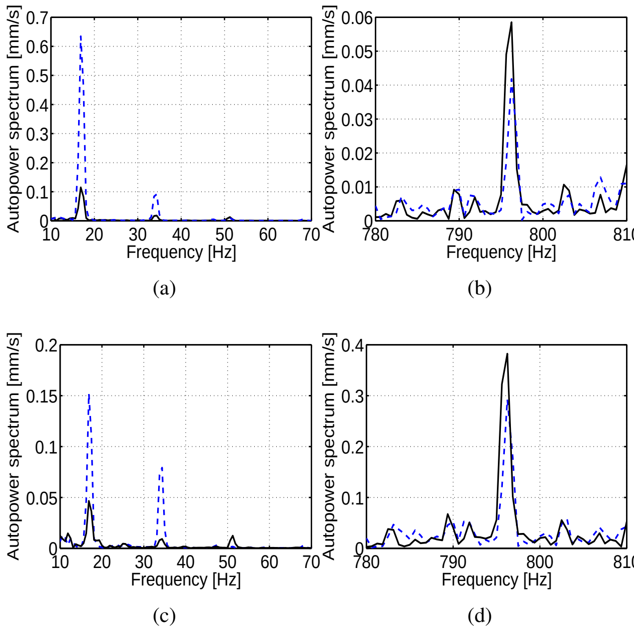

Fig. 20. Vibration velocity autopower spectrum measured at the D-end bearing. (a) and (b) x -direction, (c) and (d) y -direction, controlled system (solid line), uncontrolled system (dashed line).

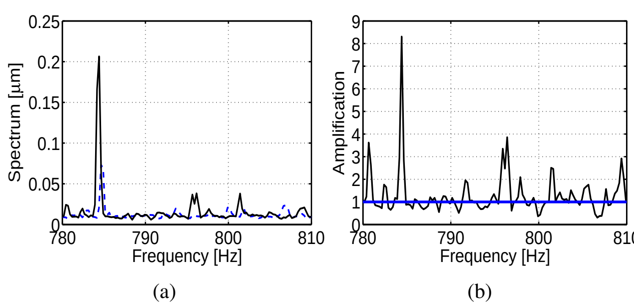

Fig. 21. Radial rotor vibration at high frequency domain; (a) vibration spectrum of the controlled system (solid line) and uncontrolled system (dashed line), (b) proportional amplification (unit amplification marked by horizontal line).

In Fig.20, velocity autopower spectra of the vibration at the D-end bearing in x and y -directions is shown. By comparing Fig.20(a) to Fig.20(b) and Fig.20(c) to Fig.20(d) it can be seen that, on contrary to x -direction, the vibration in y -direction is emphasized in the high-frequency range. Then, even though the low-frequency vibration suppression being successfull (Fig.20(c)), the vibration level has increased in y -direction due to the high-frequency amplification. The high-frequency amplification of the controller can be seen from the vibration spectrum of the radial rotor vibration, i.e. spectrum of the signal $\sqrt{x^2 + y^2}$. The results obtained by using the displacement transducers are shown in Fig.21. It can be seen that some high-frequency vibration components were amplified.

VI. Discussion and Conclusions

In this paper, attenuation of flexural rotor vibration in electrical machines was considered. Application of harmonic excitation compensation in a two-pole cage induction machine was demonstrated. A non-contact electromagnetic actuator was applied for generation of lateral force on the rotor. The main observations in this paper are

1) the algorithms for compensation of harmonic excitation provide a potential tool for low-frequency rotor vibration suppression in electrical machines,
2) the built-in force actuator is an applicable force actuation methodology to be used with the harmonic excitation compensation algorithms,
3) voltage-fed control winding and eccentric cage rotor is a coupled electromechanical system.

Based on the experiments, it was observed that the rms values of the amplitude and velocity of the flexural rotor vibration were decreased by 97.50% and 57.60%, respectively, when control was switched on. The overall vibration level (mm/s, rms) in N-end bearing was decreased by 9.10% but, on the contrary, in D-end bearing it was increased by 4.40%. In conclusion, due to the bearing block high-frequency dynamics, the vibration level in the D-end bearing was increased. Nevertheless, it was observed that (1) the vibration levels were small and (2) the problems with noise did not appear. In some applications, however, the high-frequency amplification may result in problems with noise, for instance.

In this work, the vibration attenuation was applied at no-load operating conditions. In addition, the machine was supplied by a generator which provided a smooth fundamental field compared to frequency converter supply widely used in practical applications. In order to bring the set-up closer to a real application, these aspects have to be considered. Furthermore, the identification was carried out for a fixed rotation speed and fixed two-pole flux. Changing operating conditions and online (parametric) identification belongs to future research. By increasing the two-pole field, for example, the RL -resonance damping may decrease, which causes problems in frequency-domain estimation and hence may require a pre-compensator to be used as a part of the control strategy. In the later developments, the CC algorithm coupled with a linear-quadratic feedback controller [39] provided wide frequency-band attenuation of rotor vibration including stable operation at the critical speed of the machine.

Acknowledgment

The authors gratefully acknowledge financial support from the Academy of Finland and VTT Technical Research Centre of Finland. The authors are grateful to Ari Haavisto, Helsinki University of Technology, Faculty of Electronics, Communications and Automation, for assistance in experiments and building up the experimental set-up. Special thanks are devoted to Prof. Marko Hinkkanen, Helsinki University of Technology, Power Electronics Laboratory, for guidance with the dSpace system.

REFERENCES

[1] A. Smith and D. Dorrell, "Calculation and measurement of unbalanced magnetic pull in cage induction motors with eccentric rotors. part i: Analytical model," *IEE Proceedings – Electric Power Applications*, vol. 143(3), pp. 193–201, 1996.

[2] J. Moreira and T. Lipo, "Modeling of saturated ac machines including air gap flux harmonic components," *IEEE Transactions on Industry Applications*, vol. 28(2), pp. 343–349, 1992.

[3] T. P. Holopainen, A. Tenhunen, E. Lantto, and A. Arkkio, "Unbalanced magnetic pull induced by arbitrary eccentric motion of cage rotor in transient operation, part 1: Analytical model," *Electrical Engineering (Archiv für Electrotechnik)*, vol. 88(1), pp. 13–24, 2005.

[4] U. Werner, "Rotordynamische analyse von asynchronmaschinen mit magnetischen unsymmetrien," *Diss. TU Darmstadt D17. Shaker Verlag, Aachen*, pp. 1–317, 2006.

[5] A. Arkkio, M. Antila, K. Pokki, A. Simon, and E. Lantto, "Electromagnetic force on a whirling cage rotor," *IEE Proceedings – Electric Power Applications*, vol. 147, pp. 353–360, 2000.

[6] P. Frauman, A. Burakov, and A. Arkkio, "Effects of the slot harmonics on the unbalanced magnetic pull in an induction motor with an eccentric rotor," *IEEE Transactions on Magnetics*, vol. 43(8), pp. 3441–3444, 2007.

[7] J. Faiz, B. Ebrahimi, B. Akin, and H. Toliyat, "Finite-element transient analysis of induction motors under mixed eccentricity fault," *IEEE Transactions on Magnetics*, vol. 44, no. 1, pp. 66–74, 2008.

[8] J. S. Rao, *Vibratory Condition Monitoring of Machines*. New Delhi, India: Narosa Publishing House, 2000.

[9] P. Hamer, B. Wood, J. McClurg, and W. Billington, "Large 3600 r/min induction motors operating below their first system resonant speed," *IEEE Transactions on Industry Applications*, vol. 31, no. 5, pp. 1177–1185, 1995.

[10] W. Khoo, S. Garvey, K. Kalita, and P. Houlston, "Vibration control with lateral force produced in electrical machines," *Proceedings of 8th International Conference on Vibrations in Rotating Machinery (IMechE), University of Wales, Swansea, UK, 7.-9.9.2004 (2004), 713-722*.

[11] A. Chiba, T. Fukao, O. Ichikawa, M. Oshima, M. Takemoto, and D. G. Dorrell, *Magnetic bearings and bearingless drives*. Boston, MA: Elsevier Newnes Press, 2005.

[12] A. Chiba, D. T. Power, and M. A. Rahman, "Characteristics of a bearingless induction motor," *IEEE Transactions on Magnetics*, vol. 27(6), pp. 5199–5201, 1991.

[13] A. Salazar and R. Stephan, "A bearingless method for induction machines," *IEEE Transactions on Magnetics*, vol. 29, no. 6, pp. 2965–2967, 1993.

[14] S. Khoo, R. Fittro, and S. Garvey, "An ac self-bearing rotating machine with a single set of windings," *Proceedings of International Conference on Power Electronics, Machines and Drives (Conf. Publ. No. 487)*, pp. 292–297, 2002.

[15] A. Chiba, T. Fukao, and M. Rahman, "Vibration suppression of a flexible shaft with a simplified bearingless induction motor drive," *Conference Record of the 2006 IEEE Industry Applications Conference 2006. 41st IAS Annual Meeting.*, vol. 2, pp. 836–842, 2006.

[16] C. R. Burrows and M. N. Sahinkaya, "Vibration control of multi-mode rotor-bearing systems," *Proceedings of the Royal Society of London, Series A, Mathematical and Physical Sciences*, vol. 386(1790), pp. 77–94, 1983.

[17] L. Sievers and A. von Flotow, "Linear control design for active vibration isolation of narrow band disturbances," *Proceedings of the 27th IEEE Conference on Decision and Control*, vol. 2, pp. 1032–1037, 1988.

[18] S. Hall and N. Wereley, "Linear control issues in the higher harmonic control of helicopter vibrations," *Proceedings of 45th Annuual Forum of the American Helicopter Society, Boston, USA*, pp. 955–971, 1989.

[19] C. Knospe, R. Hope, S. Fedigan, and R. Williams, "New results in the control of rotor synchronous vibration," *Proceedings of the Fourth International Symposium on Magnetic Bearings (ISMB4), vdf Hochschulverlag AG, Zurich, Switzerland, August 23-26, 1994.*

[20] P. S. Keogh, C. R. Burrows, and T. Berry, "On-Line Controller Implementation for Attenuation of Synchronous and Transient Rotor Vibration," *Journal of Dynamic Systems, Measurement, and Control*, vol. 118, pp. 315–321, 1996.

[21] E. Lantto, "Robust control of magnetic bearings in subcritical machines," *Doctoral dissertation. Acta Polytechnica Scandinavica, The Finnish academy of technology*, pp. 1–143, 1999, http://lib.tkk.fi/Diss/199X/isbn9512255758/.

[22] P. S. Keogh, M. O. T. Cole, and C. R. Burrows, "Multi-State Transient Rotor Vibration Control Using Sampled Harmonics," *Journal of Vibration and Acoustics*, vol. 124, p. 186, 2002.

[23] E. Lantto and V. Tommila, "A supercritical 250 kw industrial air compressor prototype," *The Eleventh International Symposium on Magnetic Bearings (ISMB11), Nara, Japan, August 26-29, 2008.*

[24] G. Schweitzer and E. Maslen, *Magnetic Bearings - Theory, Design, and Application to Rotating Machinery*. Berlin: Springer Verlag, 2009.

[25] K. Tammi, "Active control of radial rotor vibrations: Identification, feedback, feedforward, and repetitive control methods," *Doctoral dissertation, Helsinki University of Technology, Department of Automation and Systems Technology*, pp. 1–165, 2007, http://lib.tkk.fi/Diss/2007/isbn9789513870089/.

[26] Y. Okada, K. Dejima, and T. Ohishi, "Analysis and comparison of pm synchronous motor and induction motor type magnetic bearings," *IEEE Transactions on Industry Applications*, vol. 31, no. 5, pp. 1047–1053, 1995.

[27] P. K. Kovács, *Transient phenomena in electrical machines*. Amsterdam: Elsevier Science Publishers, 1984.

[28] A. Laiho, K. Tammi, K. Zenger, and A. Arkkio, "A model-based flexural rotor vibration control in cage induction electrical machines by a built-in force actuator," *Electrical Engineering (Archiv für Electrotechnik)*, vol. 90(6), pp. 407–421, 2008.

[29] K. J. Binns and M. Dye, "Identification of principal factors causing unbalanced magnetic pull in cage induction motors," *Proceedings of IEE*, vol. 120, no. 3, pp. 349–354, 1973.

[30] E. Maslen and J. Bielk, "A stability model for flexible rotors with magnetic bearings," *Journal of Dynamic Systems, Measurement, and Control*, vol. 114, no. 1, pp. 172–175, 1992.

[31] S. Daley, J. Hätönen, and K. Tammi, "Instantaneous harmonic vibration control of a flexible rotor," *Proceedings of the International Symposium on Active Control of Sound and Vibration, Adelaine, Australia, 18 - 20 Sept. 2006*, p. 11p, 2006.

[32] C. Knospe, R. Hope, S. Tamer, and S. Fedigan, "Robustness of adaptive unbalance control of rotors with magnetic bearings," *Journal of Vibration and Control*, vol. 2, pp. 33–52, 1996.

[33] A. Chiba and T. Fukao, "Optimal design of rotor circuits in induction type bearingless motors," *IEEE Transactions on Magnetics*, vol. 34(4), pp. 2108–2110, 1998.

[34] A. Arkkio, A. Niemenmaa, and J. Saitz, "Hysteresis torque in a cage induction motor," *International Conference on Electrical Machines (ICEM'98), Istanbul, Turkey*, pp. 1494–1499, 1998.

[35] D. Ewins, *Modal Testing: Theory and Practise*. London: Advanced Studies Press, 2000.

[36] T. Holopainen, S. Aatola, and A. Arkkio, "Vibration measurements for validation of electromechanical rotor model for cage induction motor," *Proceedings of 8th International Conference on Vibrations in Rotating Machinery (IMechE), University of Wales, Swansea, UK, 7.-9.9.2004 (2004), 423 - 432*.

[37] M.-J. Kim, B.-K. Kim, J.-W. Moon, Y.-H. Cho, D.-H. Hwang, and D.-S. Kang, "Analysis of inverter-fed squirrel-cage induction motor during eccentric rotor motion using fem," *IEEE Transactions on Magnetics*, vol. 44, no. 6, pp. 1538–1541, 2008.

[38] A. Sinervo, "Modeling and control of flexural rotor vibration of a two-pole cage induction motor," Master's thesis, Helsinki University of Technology, Faculty of electronics, Communications and Automation, Department of electrical Engineering, Espoo, Finland, 2008.

[39] J. Orivuori, A. Laiho, A. Sinervo, K. Zenger, and A. Arkkio, "Suppression of rotor vibrations of an electric machine at the critical speed by optimal state feedback controller," *The European Control Conference 2009, Budapest, Hungary, August 23-26, 2009 (in press).*

Antti Laiho was born in Helsinki, Finland, in 1977. He received M.Sc.(Tech.) degree from Helsinki University of Technology, Finland, in 2003. His research interests involve electromechanical interactions, structural analysis and active control of vibrations. He is currently working as research scientist in VTT Technical Research Centre of Finland.

Anssi Sinervo was born in Helsinki, Finland, in 1984. He received M.Sc.(Tech.) degree from Helsinki University of Technology, Finland, in 2008. His research interests involve time-periodic modeling of electrical machines and air-gap flux harmonics caused by rotor eccentricity. He is currently pursuing post-graduate studies and working as a research scientist in Helsinki University of Technology in Electromechanics.

Juha Orivuori was born in Helsinki, Finland, in 1981. He received M.Sc.(Tech.) degree from Helsinki University of Technology, Finland, in 2008. His research interests involve optimal control and active control of vibrations. He is currently working as research scientist in the Department of Automation and Systems Technology at Helsinki University of Technology

Kari Tammi was born in Espoo, Finland, in 1974. He received M.Sc, Lic.Sc and D.Sc. (Tech.) degrees from Helsinki University of Technology in 1999, 2003 and 2007, respectively. His research interests involve dynamic systems, electrical machines and active control. He is currently working as a team leader at VTT, Finland.

Antero Arkkio was born in Vehkalahti, Finland in 1955. He received his M.Sc. (Tech.) and D.Sc. (Tech.) degrees from Helsinki University of Technology, Finland, in 1980 and 1988, respectively. He has been a Professor of electrical engineering (Electromechanics) at Helsinki University of Technology (TKK) since 2001. Before this, he was a Senior Research Scientist and Laboratory Manager at TKK. He has worked with various research projects dealing with modeling, design, and measurement of electrical machines.

Kai Zenger was born in Helsinki, Finland, in 1958. He received the M.Sc. degree in electrical engineering in 1986, and Lic.Sc. and D.Sc. degrees in 1992 and 2003, respectively. After an industrial career he has had different positions at Helsinki University of Technology, where he currently works as a Senior Researcher in the Department of Automation and Systems Technology. His main research areas are Control Engineering and System Theory generally, with applications in chemical process engineering, power electronics and mechanical engineering. He has specialized in the research of time-varying linear systems, periodic systems and adaptive and robust control methods.